NOLTA, IEICE

Paper

Experimental manipulation of intrinsic localized modes in macro-mechanical system

Masayuki Kimura [1a)] *and Takashi Hikihara* [2b)]

[1] *School of Engineering, The University of Shiga Prefecture 2500 Hassaka-cho, Hikone, Shiga 522-8533, Japan*

[2] *Department of Electric Engineering, Kyoto University Katsura, Nishikyo-ku, Kyoto 615-8510, Japan*

[a)] *kimura.m@e.usp.ac.jp*
[b)] *hikihara@kuee.kyoto-u.ac.jp*

Received May 23, 2011; Revised November 20, 2011; Published April 1, 2012

Abstract: A macro-mechanical cantilever array is proposed for experimental investigation of intrinsic localized modes (ILMs). The array is designed to have tunable on-site potentials that can be adjusted individually. Thus, it is easy to realize an array, in which an ILM can be excited. In addition, impurities can be induced in and removed from the array. Several ILMs were successfully generated by an external sinusoidal excitation, and the generated ILMs were manipulated by adding an impurity to the cantilever array. The manipulation mechanism is discussed numerically on the basis of the structure of phase space. Coexisting ILMs, unstable manifolds, and the domains of attraction of a stable ILM are shown for an ILM manipulated by adding an impurity.

Key Words: intrinsic localized mode, discrete breather, coupled cantilever array, manipulation

1. Introduction

Energy localized vibration in a nonlinear lattice was first discovered by Sievers and Takeno in 1988 [17]. Such localized vibration in discrete media is now called an intrinsic localized mode (ILM) or discrete breather (DB). In this decade, ILMs have been identified in many types of physical systems, for instance, Josephson-junction arrays [1, 19, 20], optical wave guides [4, 11], photonic crystals [7], a micro-mechanical cantilever array [14], mixed-valence transition metal complexes [9, 18], antiferromagnets [15], and electronic circuits [5, 16]. Experiments with micro-cantilever arrays can facilitate the application of ILMs to micro- or nano-engineering because cantilever structures are widely used in micro and nano devices [21]. Thus, ILMs in a micro-cantilever array have the potential to be used for sensors and actuators requiring high sensitivity and accuracy.

Control of an ILM involves manipulating its appearance, disappearance, and spatial position along a particular direction and applying these properties in sensor and actuator modes. Sato *et al.* [13]

Nonlinear Theory and Its Applications, IEICE, vol. 3, no. 2, pp. 233–245 DOI: 10.1588/nolta.3.233

reported experimental manipulation of micro-cantilever arrays. ILMs were generated, destroyed, repelled, and attracted by adding a localized impurity; thus, demonstrating the possibility of indirectly controlling ILMs by positioning a local impurity in the array.

The mechanism by which ILMs are manipulated is generally governed by the structure of the phase space under control. Experimental investigations could illuminate the conjectured mechanism phenomenologically. Macrosystems offer advantages for grasping their dynamics and achieving a method of controlling ILMs, if analogous features in macrosystems are qualitatively retained in ILMs. Here we introduce a macro-cantilever array system that exhibits ILMs similar to those of micro or nanosystems.

One of the authors proposed a magneto-elastic beam model for describing nonlinearly coupled Duffing-type pendulums [8]. The model was used to investigate waves and vibrations in nonlinearly coupled pendulums. The experimental model has a similar equation of motion to the micro-cantilever array in which ILMs were observed. In the model, permanent magnets are placed so as to adjust the on-site nonlinearity. If the magnetic field is adjustable at each site, an impurity can be added or released. This concept inspired us to develop a magneto-elastic beam system with tunable electromagnets. In this paper, we first introduce the macro-mechanical cantilever array and model it as nonlinear coupled ordinary differential equations. In Sec. 3, we present experimental observations of ILMs. The experimental results are confirmed by a numerical simulation. In addition, the coexistence and stability of ILMs are investigated. Experimental manipulations of ILMs are demonstrated in Sec. 4; a standing ILM is attracted to a manually created impurity. The mechanism for the manipulation is discussed numerically in terms of the phase structure.

2. Cantilever array

2.1 Cantilever with cylindrical magnet

In this section, the equation of motion of a cantilever is derived. Figure 1 shows a schematic configuration of the cantilever. A cylindrical mass is attached at the free end of the cantilever. The cantilever's vibration is described by the Euler-Bernoulli beam theory as

$$\rho w h \frac{\partial^2 y}{\partial t^2} = -EI \frac{\partial^4 y}{\partial x^4}, \tag{1}$$

where y represents the displacement of the cantilever at a position x away from the equilibrium position. The moment of inertia is represented by $I = wh^3/12$. The solution of Eq. (1) is assumed to be $y(x,t) = Y(x)\sin(\omega_0 t)$. Next, the ordinary differential equation

$$\frac{\mathrm{d}^4 Y}{\mathrm{d}x^4} = -\frac{\rho w h}{EI}\omega_0^2 Y, \tag{2}$$

which can be easily solved, is obtained. The general solution with four arbitrary constants is

$$Y(x) = C_1 \sin\left(\frac{\lambda}{\ell}x\right) + C_2 \cos\left(\frac{\lambda}{\ell}x\right) + C_3 \sinh\left(\frac{\lambda}{\ell}x\right) + C_4 \cosh\left(\frac{\lambda}{\ell}x\right), \tag{3}$$

where λ is a nondimensional parameter defined as $\lambda^2 = \ell^2 \omega_0 \sqrt{\rho w h / EI}$. The boundary conditions for the cantilever are

$$\begin{aligned} &\begin{cases} Y(0) = 0 \\ Y'(0) = 0 \end{cases} \quad \text{for the fixed end,} \\ &\begin{cases} EIY'''(\ell) + m\omega_0^2 Y(\ell) = 0 \\ -EIY''(\ell) + J\omega_0^2 Y'(\ell) = 0 \end{cases} \quad \text{for the free end,} \end{aligned} \tag{4}$$

where m and J denote the mass and moment of the cylindrical magnet, respectively. The boundary conditions yield $C_1 = -C_3,\ C_2 = -C_4$ and the condition

$$\begin{aligned} &(1 + \cos\lambda\cosh\lambda) - \frac{\lambda^3}{\ell^3}\frac{J}{\rho A}(\sin\lambda\cosh\lambda + \cos\lambda\sinh\lambda) \\ &- \frac{\lambda}{\ell}\frac{M}{\rho A}(\sin\lambda\cosh\lambda - \cos\lambda\sinh\lambda) + \frac{MJ}{\rho^2 A^2}\frac{\lambda^4}{\ell^4}(1 - \cos\lambda\cosh\lambda) = 0, \end{aligned} \tag{5}$$

Fig. 1. Configuration of cantilever with permanent magnet.

which determines the frequency of the vibrating cantilever. The lowest value of λ satisfying Eq. (5) is numerically obtained as about $1.64 (= \lambda_1)$[1]. The shape function $Y(x)$ shows that the end of the cantilever oscillates with the largest amplitude. This oscillation is called the first mode oscillation of the cantilever. This paper focuses on the first mode so that the partial differential equation is reduced to an ordinary differential equation.

When the cantilever oscillates at the first mode frequency ω_0, the displacement of its end is a simple harmonic oscillation $y(\ell, t) = Y(\ell)\sin(\omega_0 t)$. On the basis of the harmonic oscillation of a linear spring?mass system without damping, the motion of the end of the cantilever is described by

$$\ddot{u} = -\omega_0^2 u, \tag{6}$$

where u denotes the displacement of the tip of the cantilever. Equation (6) represents the linear oscillation of the tip of cantilever for a small amplitude.

2.2 Magnetic interaction

A cylindrical permanent magnet (PM) is attached to the free end of the cantilever. The restoring force between the PM and an electromagnet (EM) placed below produces nonlinear interaction. The configuration is shown in Fig. 2. For simplicity, we assume that the magnetic force between the PM and the EM can be approximately described by Coulomb's law for magnetic charges. The configuration of the magnetic charges is shown in Fig. 2(b). If the cantilever's displacement is sufficiently small relative to its length, Coulomb's law for magnetic charges gives

$$\begin{aligned} F(u) =& \frac{m_\mathrm{p} m_\mathrm{e}}{4\pi\mu_0} \frac{u}{(u_0^2 + d_0^2)^{\frac{3}{2}}}, \\ =& \chi(I_\mathrm{EM}) \frac{u}{(u_0^2 + d_0^2)^{\frac{3}{2}}}, \end{aligned} \tag{7}$$

where m_p and m_e correspond to the magnetic charges of the PM and EM, respectively. The distance between the magnets is denoted by d_0 in the equilibrium state. The magnetic permeability is represented by μ_0. Because the magnitude of m_e depends on the current flowing in the EM, the coefficient of the interaction can be represented as a function of the current $\chi(I_\mathrm{EM})$. In this paper, we assumed the linear relationship $\chi(I_\mathrm{EM}) = \chi_0 + \chi_1 I_\mathrm{EM}$. An attractive force between the magnets appears even if the current is zero because the EM has a ferromagnetic core. Thus, χ_0 is always negative. On the other hand, the current direction changes the sign of $\chi_1 I_\mathrm{EM}$. The current direction is defined as positive when it enhances the attractive force. Therefore, χ_1 is also negative.

A voice coil motor is attached to excite the cantilever, as shown in Fig. 2. When the voice coil motor is driven by a sinusoidal signal, the motion of the cantilever is given by

$$\ddot{u} = -\,\omega_0^2 u - \gamma\dot{u} + F(u) + A\cos(\omega t), \tag{8}$$

where A and ω denote the magnitude and angular frequency, respectively, of the external force excited by the voice coil motor. The damping coefficient γ is required because of air resistance.

2.3 Frequency response of cantilever

The restoring force on each cantilever varies nonlinearly because of the magnetic interaction force between the PM and the EM. Figure 3(a) shows the relationship between the amplitude and the

[1]The corresponding frequency is about 37.5 Hz.

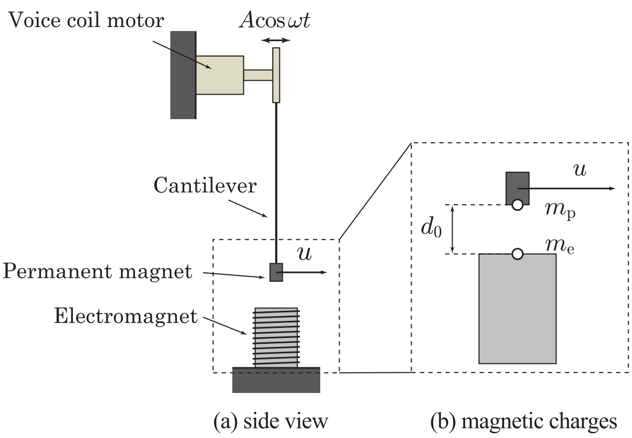

Fig. 2. (a) Side view of cantilever. A permanent magnet is attached at its free end. An electromagnet is placed beneath the permanent magnet. (b) Magnetic charge configuration.

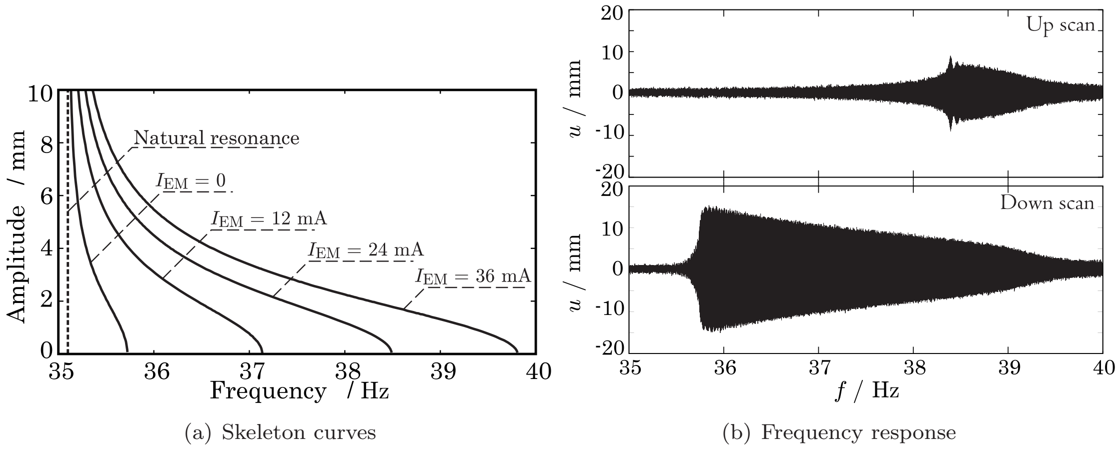

Fig. 3. (a) Skeleton curves. Each curve was obtained numerically. (b) Frequency response for $I_{EM} = 24\,\mathrm{mA}$.: up scan(top) and down scan(bottom). Scan rate was $0.05\,\mathrm{Hz/s}$. Estimated damping and external force were $\gamma = 1.5\,\mathrm{s}^{-1}$ and $A = 3.0\,\mathrm{m/s^2}$, respectively.

frequency when both γ and A are 0. The shapes of the skeleton curves demonstrate the soft-spring characteristics of the cantilever. The curves in Fig. 3(a) asymptotically approach the line representing the natural frequency of the cantilever as the amplitude increases because the contribution of the magnetic interaction becomes small when the amplitude is larger than the diameter of the EM. On the other hand, the frequency at small amplitudes depends strongly on the current flowing in the EM. The linearization of Eq. (10) gives a resonant frequency of

$$\omega_0' = \sqrt{\omega_0^2 - (\chi_0 + \chi_1 I_{EM})/d_0^3}, \tag{9}$$

where χ_0 and χ_1 are assumed to be negative. The resonant frequency shifts to the high frequency side with increasing current.

The experimental frequency responses clearly show a hysteretic response with respect to the external force at frequencies below the resonant frequency, as shown in Fig. 3(b). The cantilever's amplitude increased rapidly at 38.3 Hz during the up scan of the frequency. However, during the down scan, the amplitude jump occurred at 35.9 Hz. In terms of its phenomenological behavior, the cantilever has two stable states when the frequency of the external excitor is between 35.9 Hz and 38.3 Hz. To excite a localized oscillation, the external excitor should vibrate the array with a frequency at which hysteresis occurs [12]. We adopted a frequency of 36.1 Hz for the external excitor in order to excite ILMs.

2.4 Mechanically coupled cantilevers

Adjacent cantilevers are coupled by attaching an elastic rod called the coupling rod. Figure 4 shows a schematic of the macro-mechanical cantilever array's configuration; Table I lists its specifications. Eight cantilevers were placed at equal intervals along one dimension. The cantilevers were derived using Eq. (8), and each was mechanically coupled by the coupling rod. The coupling rod produces a force that depends on the differences in the displacements of adjacent cantilevers. The force changes linearly with respect to the displacement difference if the deformation of the rod is sufficiently small. As shown in Fig. 4, the rod is attached near the support. The displacement of the cantilever at the rod is quite small relative to that at the tip, so we assume that the coupling force is linear. Therefore, the equation of motion of the coupled cantilever array is

$$\begin{cases} \dot{u}_n = v_n, \\ \dot{v}_n = -\omega_0^2 u_n - \gamma u_n + F(u_n) + A\cos(\omega t) \\ \qquad\quad - C(u_n - u_{n+1}) - C(u_n - u_{n-1}), \end{cases} \tag{10}$$

where $n = 1, 2, \ldots, 8$ and C denotes a constant coupling coefficient. As shown in Fig. 4, a short, wide cantilever is attached at either end of the array to form fixed boundaries. Therefore, the boundary conditions of Eq. (10) are

$$\begin{cases} u_0 = 0, \quad v_0 = 0, \\ u_9 = 0, \quad v_9 = 0. \end{cases} \tag{11}$$

The natural frequency of the cantilever without the electromagnet is experimentally determined to 35.1 Hz by taking the frequency response at small amplitude excitation. The peak frequency corresponds to ω_0. The damping coefficient was estimated at $1.5\,\mathrm{s}^{-1}$ by measuring the decay rate of

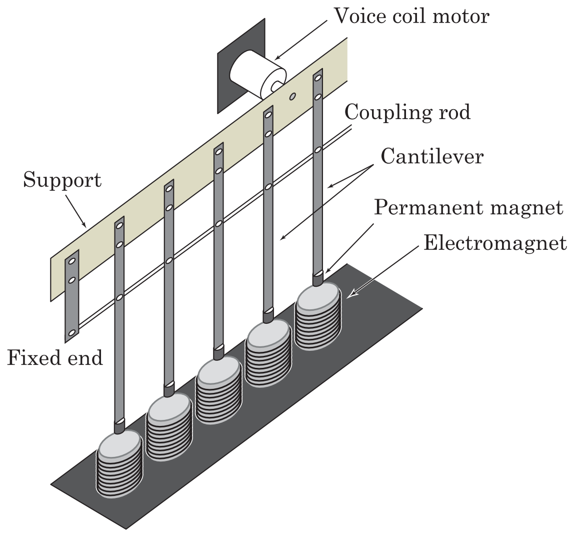

Fig. 4. Overview of the cantilever array. Eight cantilevers are mechanically coupled by the coupling rod. Short cantilever is attached at the end of the array to realize a fixed boundary condition. Voice coil motor excites the entire array except for the electromagnets.

Table I. Specifications of cantilever array.

Each cantilever			
Length(ℓ)	70.0 mm	Width(w)	5.0 mm
Thickness(h)	0.3 mm	Pitch(p)	15.0 mm
Density(ρ)	8.0×10^3 kg/m^3	Young's modulus(E)	197 GPa

Cylindrical magnet			
Radius (r)	1.5 mm	Height(l)	3.0 mm
Mass (m)	96.6 mg		

Table II. List of symbols in Eq. (10).

Symbol	Value	Symbol	Value
ω_0	$2\pi\times 35.1$ rad/s	γ	$1.5\ \mathrm{s}^{-1}$
C	$284\ \mathrm{s}^{-2}$	χ_0	$-4.71\times 10^{-5}\ \mathrm{m}^3/\mathrm{s}^2$
d_0	3.0 mm	χ_1	$-9.14\times 10^{-3}\ \mathrm{m}^3/\mathrm{s}^2\mathrm{A}$
A	$3.0\ \mathrm{m/s}^2$	ω	$2\pi\times 36.1$ rad/s

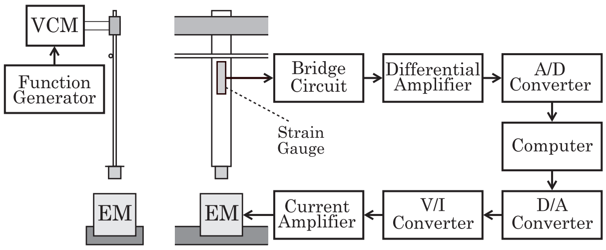

Fig. 5. Experimental setup.

amplitude when the driving force turned off. For the nonlinear term, the shift of resonant frequency was measured to determine χ_0 and χ_1. As shown in Eq. (9), $\omega_0'^2$ increases linearly as the current increases if χ_0 and χ_1 are negative. We obtained $\chi_0 = -4.71\times 10^{-5}\,\mathrm{m}^3/\mathrm{s}^2$ and $\chi_1 = -9.14\times 10^{-3}\,\mathrm{m}^3/\mathrm{s}^2\mathrm{A}$ by applying the lease square method to measured values. The coupling coefficient C was determined by vibrating the array with small amplitude, where electromagnets were removed because they affect the restoring force of cantilevers even though no current flows. The frequency difference between the lowest mode and the highest mode was measured by slowly sweeping the driving frequency. All adjacent cantilevers oscillate in-phase at the lowest mode and anti-phase at the highest mode. The frequency of the lowest mode approximately corresponds to ω_0 while the coupling is weak. For the same reason, the highest mode frequency can be assumed to be $\sqrt{\omega_0^2+4C}$. Therefore, the coupling coefficient can be estimated by $C = \frac{1}{4}(\Delta_\omega^2 + 2\omega_0\Delta_\omega)$, where Δ_ω represent the frequency different and was measured as $2\pi\times 2.50\,\mathrm{rad/s}$. As a result, the coupling coefficient is obtained as $C = 284\,\mathrm{s}^{-2}$, which is relatively small compared with ω_0^2. The array is thus in the weak coupling regime. The experimentally estimated parameters are listed in Table II.

2.5 Experimental setup

The experimental setup is shown in Fig. 5. The displacement of each cantilever u_n is measured using a strain gauge. The resistance of the strain gauge changes slightly with the displacement of the cantilever. To detect the small change in resistance, a bridge circuit with a differential amplifier was used. The amplified voltage signal was stored in a computer via a multi-channel A/D converter. The current flowing in each EM was adjusted individually by the computer. The computer generates a voltage signal via a multi-channel D/A converter. A V/I converter including a current amplifier supplied current to the EM.

To excite the cantilever array, the voice coil motor was attached to the support as shown in Fig. 5. The motor was driven by a sinusoidal voltage signal generated by a function generator.

3. Intrinsic localized mode

3.1 Observation of localized oscillations

The frequency of the external excitor should be set to that at which hysteresis of the frequency response occurs [12]. Thus, we chose a frequency of 36.1 Hz on the basis of the experimental results shown in Fig. 3(b). Since each cantilever has two stable solutions, large- and small-amplitude oscillations, no ILM was observed when the excitor was first turned on. The corresponding wave form is shown in Fig. 6(a). All the cantilevers oscillated in phase with small amplitude. We manually percussed a cantilever in order to excite an ILM and successfully observed several localized oscillations. Figures 6(b), (c), and (d) show the wave forms of the observed ILMs. One of the cantilevers has quite large amplitude, whereas the others have relatively small amplitudes. The amplitude distribution

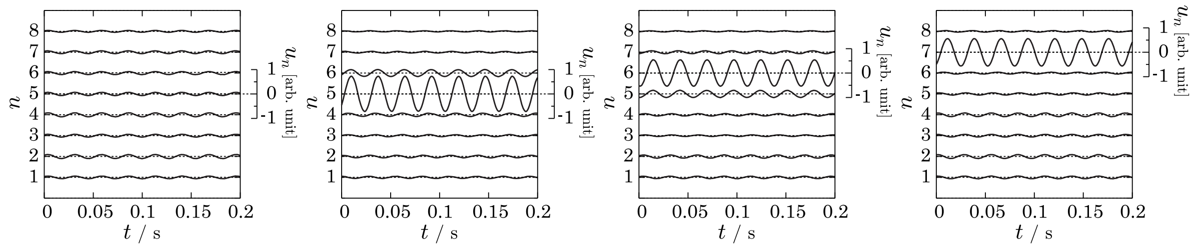

(a) No ILM (b) ILM at $n = 5$ (c) ILM at $n = 6$ (d) ILM at $n = 7$

Fig. 6. Experimentally excited ILMs: (a) no ILM; ILMs excited at (b) $n = 5$, (c) $n = 6$, and (d) $n = 7$. Cantilever array was subjected to external vibration at 36.1 Hz.

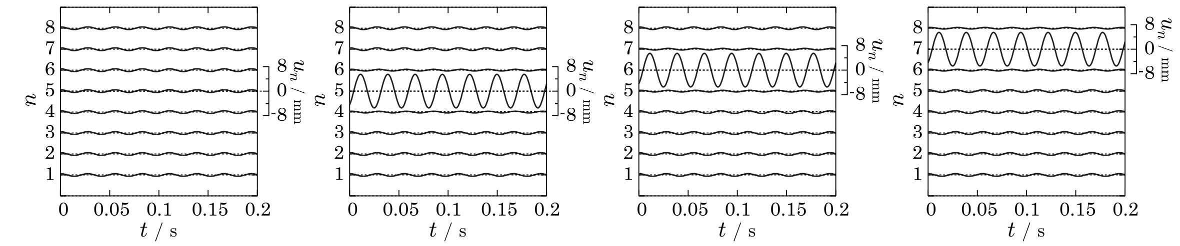

(a) No ILM (b) ILM at $n = 5$ (c) ILM at $n = 6$ (d) ILM at $n = 7$

Fig. 7. ILMs obtained by numerically using Eq. (10). Parameters are listed in Table II.

is obviously localized. The results of numerical calculation are shown in Fig. 7. The forth-order Runge-Kutta method was applied to integrate Eq. (10). The state with no ILM is shown in Fig. 7(a). Numerically calculated ILMs corresponding to those observed are shown in Figs. 7(b), (c), and (d). The wave forms and spatial distributions agree with the experimental results in Fig. 6. This implies that Eq. (10) has sufficient validity for discussing ILMs in the cantilever array.

In the experiment, other ILMs centered at $n = 2$ and $n = 4$ were observed. However, an ILM could not be excited at $n = 3$. The reason seems to be a disorder of the cantilever array, which is mainly caused by the variability of the length of cantilevers, the mass of permanent magnets, and the magnitude of magnetic charges. The parameters in Eq. (10) are slightly different from each other due to the disorder. The existence of disorder is implied by the spatial symmetry of the amplitude distribution. As shown in both Fig. 6(b) and Fig. 7(b), the amplitude of the sixth cantilever is larger than that of the fourth. The difference in the amplitude of the central cantilever between Figs. 6(b) and (c) also indicates the array's disorder. The disorder may change the resonant frequency of the cantilevers. As shown in Fig. 3, if the frequency of the excitor is fixed, the amplitude somewhat varies with the change in the resonant frequency. Therefore, the braking symmetry seems to be due to the disorder.

Although the numerical simulation indicate that ILMs exist at nearby the boundaries of the array, standing ILMs at $n = 1$ and $n = 8$ were not observed experimentally. It seems that the boundaries of the experimental array are not completely fixed, whereas we assumed those to be fixed. From the point of view of producing a new experimental system for investigation of the qualitative dynamics of ILM, the cantilevers attached to the ends of array should be replaced by stiffer ones to improve the fixedness of the boundaries.

3.2 Coexisting ILMs and their stability

In the experimentally observed ILMs, only one cantilever exhibited large-amplitude oscillations. These ILMs are stable because they did not decay for a long period and survived against disturbance caused by air flow around the cantilever array. On the other hand, other types of localized oscillations, which may be unstable, also exist in the cantilever array under the conditions listed in Table II. The anticontinuous limit [10] was used for obtaining ILMs. The coupling coefficient is, at first, set at $C = 0$.

If the driving frequency is chosen in the frequency region where two stable and one unstable periodic solutions coexist, a trivial localized solution can be obtained for the no-coupling regime. That is, one cantilever is set to stable or unstable resonance while the others are set to the small amplitude stable solution. Next, the coupling coefficient is slightly increased. The localized solution in the no-coupling regime is used as an initial condition of the shooting method which is the Newton-Raphson method for periodic solution. If the calculation successfully converges, the coupling coefficient is increased again. By iterating these procedure, several types of ILM were obtained, shown in Fig. 8(a). This figure corresponds to the experimentally observed ILM shown in Fig. 6(b). The label ST5$^{\mathrm{s}}$ indicates the Sievers-Takeno mode obtained under the anticontinuous limit when the fifth cantilever is set to the stable resonance. P4$^{\mathrm{s}}$-5$^{\mathrm{s}}$ is the Page mode standing between $n = 4$ and $n = 5$. As shown in Fig. 8(b), in the P mode, two cantilevers resonate. In the anticontinuous limit, the fourth and fifth cantilevers are set to the stable resonance to obtain P4$^{\mathrm{s}}$-5$^{\mathrm{s}}$. That is, the label includes two numbers with a superscript "s." Figures 8(c) and 8(d) were obtained by starting with unstable resonance in the anticontinuous limit. They are labeled ST5$^{\mathrm{u}}$ and P4$^{\mathrm{u}}$-5$^{\mathrm{u}}$, respectively. The phase of the excited oscillator for ST$^{\mathrm{u}}$ differs from that for ST$^{\mathrm{s}}$.

The Floquet multipliers for coexisting ILMs are estimated in Fig. 9. Only ST5$^{\mathrm{s}}$ is stable because all the Floquet multipliers are within a unit circle on the complex plane. This corresponds to the experimental results. On the other hand, ST5$^{\mathrm{u}}$ is unstable even though its amplitude distribution is similar to that of ST5$^{\mathrm{s}}$. The instability of ST5$^{\mathrm{u}}$ seems to originate from the unstable resonant solution in the initial condition of the anticontinuous limit. Although P4$^{\mathrm{s}}$-5$^{\mathrm{s}}$ is obtained from two

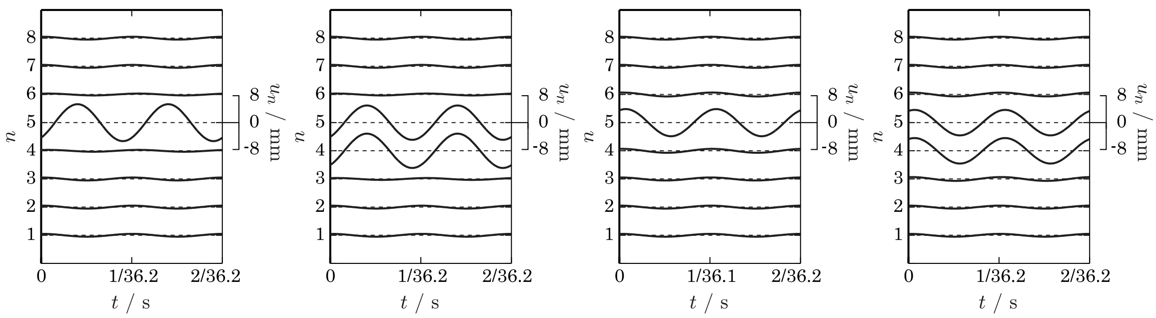

(a) ST5$^{\mathrm{s}}$ (b) P4$^{\mathrm{s}}$-5$^{\mathrm{s}}$ (c) ST5$^{\mathrm{u}}$ (d) P4$^{\mathrm{u}}$-5$^{\mathrm{u}}$

Fig. 8. ST and P modes obtained using the anticontinuous limit.

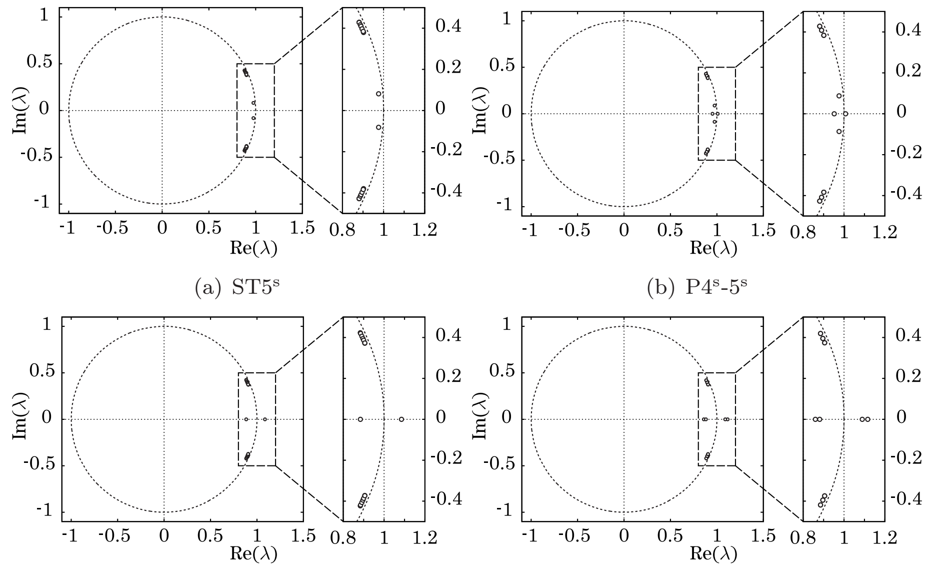

(a) ST5$^{\mathrm{s}}$ (b) P4$^{\mathrm{s}}$-5$^{\mathrm{s}}$

(c) ST5$^{\mathrm{u}}$ (d) P4$^{\mathrm{u}}$-5$^{\mathrm{u}}$

Fig. 9. Floquet multipliers of ILMs shown in Fig. 8. Left panel in each case shows enlarged area around +1 on unit circle.

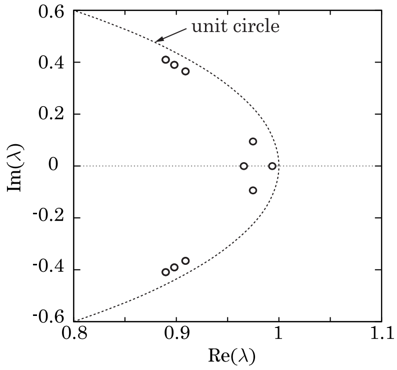

Fig. 10. Floquet multipliers of P4$^{\mathrm{s}}$-5$^{\mathrm{s}}$ when the driving frequency is set at $\omega = 2\pi \times 36.2\,\mathrm{rad/s}$.

stable resonant solutions, it has a Floquet multiplier outside the unit circle. Since P4$^{\mathrm{s}}$-5$^{\mathrm{s}}$ is unstable at $\gamma = 0$ and $A = 0$, that is, in a conservative system, P modes are unstable because of their spatially symmetric amplitude distribution. In general, the ST mode is stable and the P mode is unstable in nonlinear Klein-Gordon lattices [3]. The cantilever array proposed in this paper is classified as a nonlinear Klein-Gordon lattice because cantilevers having a nonlinear restoring force are linearly coupled with each other. Therefore, the P modes are unstable and could not be excited experimentally. P4$^{\mathrm{u}}$-5$^{\mathrm{u}}$ is obtained by two unstable resonant solutions. The spatial symmetry and the initial condition affect the stability of P4$^{\mathrm{u}}$-5$^{\mathrm{u}}$. Thus, two of its Floquet multipliers are outside the unit circle.

As shown in Fig. 9(b), P4$^{\mathrm{s}}$-5$^{\mathrm{s}}$ is unstable. However, the absolute value of the Floquet multiplier that is outside the unit circle is very close to +1. If the driving frequency is slightly larger, the multiplier enters the unit circle, as shown in Fig. 10. Thus, P4$^{\mathrm{s}}$-5$^{\mathrm{s}}$ gains stability. This implies that it is possible to excite the P modes experimentally.

The anticontinuous limit allows us to predict the existence of P4$^{\mathrm{u}}$-5$^{\mathrm{s}}$ or P4$^{\mathrm{s}}$-5$^{\mathrm{u}}$. In fact, they also coexist with other ST and P modes under a very weak coupling regime. However, such solutions disappear before the coupling coefficient reaches $C = 284\,\mathrm{s}^{-2}$.

4. ILM manipulation

4.1 ILM excitation

ILMs are usually excited by modulational instability [6, 14]. However, the position and number of ILMs cannot be predicted because modulational instability causes random behavior in traveling ILMs [2]. On the other hand, adding an impurity to the array enables the excitation of an ILM anywhere [13]. Here we consider ILM excitation using an impurity in the cantilever array. We first assume that the frequency of the external excitor is sufficiently lower than the linear resonant frequency of each cantilever. If a cantilever's resonant frequency is decreased only by adding an impurity, it will resonate. As a result, a spatially localized oscillation appears. The impurity should be removed while maintaining the localized oscillation. If the localized oscillation remains after the impurity is removed, it becomes an ILM. The experimental result of ILM excitation is shown in Fig. 11(a). The current flowing in the EM at $n = 4$ was decreased from 24.0 mA to 11.5 mA at $t = 0.88$ s. The amplitude of the fourth cantilever then began to increase. The current was increased to the original value when the amplitude became large. As a result, an ILM was excited at $n = 4$. The excitation process is called seeding [16].

4.2 Attractive manipulation of ILMs

The impurities that can excite an ILM also attract an ILM excited by other means. Figure 11(b) demonstrates attractive manipulation using an impurity. ST5$^{\mathrm{s}}$ was initially excited by the manipulation. After the impurity was added, the amplitude of the fourth cantilever began to increase while that of the fifth decreased. The impurity was removed when the amplitudes of the fourth and fifth cantilevers were almost the same. The oscillation of the fifth cantilever decreased with the spread of

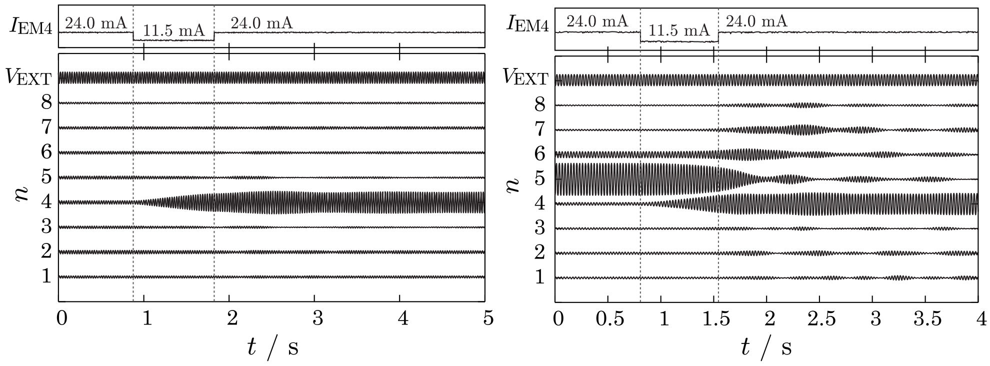

(a) Excitation

(b) Manipulation

Fig. 11. (a) ILM generation by adding an impurity. Impurity was added at $n = 4$ by changing the current I_{EM4} from 24.0 mA to 11.5 mA. (b) Manipulation of an ILM by adding the same impurity as in (a). Impurity was added at $t = 0.81$ s and removed at $t = 1.55$ s for both cases.

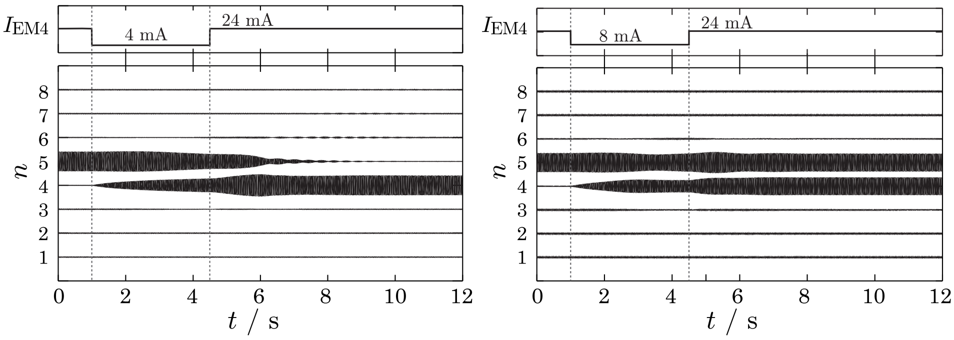

(a) Attractive manipulation

(b) Manipulation failed

Fig. 12. Numerical simulation of the attractive manipulation. (a): The current flowing in EM at $n = 4$ is decreased to 4 mA when the impurity is added. The impurity is added at $t = 1$ s and removed at $t = 4.5$ s. The amplitude and the frequency of external excitor are set at $A = 3$ m/s^2 and $\omega = 2\pi \times 35.7$ rad/s. (b): The frequency of external excitor is set at $\omega = 2\pi \times 36.2$ rad/s. The current flowing in EM at $n = 4$ is decreased to 8 mA from 24 mA when the impurity is added in this case. The impurity is added at $t = 1$ s and removed at $t = 4.5$ s. The other parameters are same as in Table II.

small traveling waves. However, the amplitude of the fourth cantilever grew large. As a result, the locus of the ILM was drawn from $n = 5$ to $n = 4$.

Attractive manipulation can also be demonstrated numerically. Figure 12(a) shows a simulation, in which the current flowing in the EM at $n = 4$ was reduced from 24 mA to 4 mA at $t = 1$ s. The amplitude of the fourth cantilever began to increase. The impurity caused by the reduced current was removed at $t = 4.5$ s. The amplitude of the fourth cantilever became almost the same as that of the fifth cantilever and then became large as the oscillation of the fifth cantilever decreased. Consequently, ST5^{s} was attracted by the impurity, as in the experimental result.

However, attractive manipulation is not always possible. An example of failed manipulation is shown in Fig. 12(b). The frequency of the external excitor and the lower value of the current were set at $\omega = 2\pi \times 36.2$ rad/s and 8 mA, respectively. The other parameters are the same as in Fig. 12(a). Until the impurity was removed, the behaviors of each cantilever were similar to those in Fig. 12(a). However, the amplitude of the fifth cantilever did not decay after the impurity was removed. Finally, P4^{s}-5^{s} remained. That is, ST5^{s} became P4^{s}-5^{s} instead of ST4^{s}. This suggests that P4^{s}-5^{s} became stable at $\omega = 2\pi \times 36.2$ rad/s. In fact, all the Floquet multipliers of P4^{s}-5^{s} are inside the unit circle. This implies that the unstable P4^{s}-5^{s} mode and the phase structure around it are particularly important for ILM manipulation.

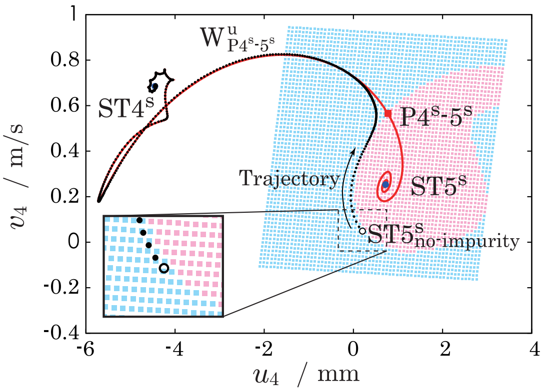

Fig. 13. Phase structure around ST5$^{\mathrm{s}}$ with an impurity, which is obtained by taking the stroboscopic mapping at $\omega t \mod 2\pi = 0$. Solid squares and circles indicate coexisting ILMs. Red solid curves represent unstable manifolds of P4$^{\mathrm{s}}$-5$^{\mathrm{s}}$ which is labeled as $W^{\mathrm{u}}_{\mathrm{P4^s\text{-}5^s}}$. Blue and red regions correspond to domains of ST4$^{\mathrm{s}}$ and ST5$^{\mathrm{s}}$ attraction, respectively. The black open circle represents ST5$^{\mathrm{s}}_{\mathrm{no-impurity}}$ and black solid circles show the trajectory.

4.3 Unstable manifolds and domains of attraction

Attractive manipulation is due to the change in the phase structure caused by adding an impurity. Figure 13 shows the phase structure when an impurity exists at $n = 4$. The impurity was induced by decreasing the current I_{EM4} to 5 mA. ST4$^{\mathrm{u}}$, ST5$^{\mathrm{u}}$, and P4$^{\mathrm{s}}$-5$^{\mathrm{s}}$ survived at $I_{\mathrm{EM4}} = 4$ mA and vanished when the impurity was added. ST5$^{\mathrm{s}}$ in the no-impurity regime (ST5$^{\mathrm{s}}_{\mathrm{no-impurity}}$) is indicated by the open circle. The domains of attraction were calculated for phase points on the plane that includes P4$^{\mathrm{s}}$-5$^{\mathrm{s}}$, ST5$^{\mathrm{s}}$, and ST5$^{\mathrm{s}}_{\mathrm{no-impurity}}$. The blue and red regions correspond to the domains of attraction of ST4$^{\mathrm{s}}$ and ST5$^{\mathrm{s}}$, respectively. The boundary between them seems to be formed by the stable manifold of P4$^{\mathrm{s}}$-5$^{\mathrm{s}}$. As a result of the added impurity, the open circle moved into the blue region (Fig. 13, inset). The trajectory shown with solid circles in Fig. 13 approaches P4$^{\mathrm{s}}$-5$^{\mathrm{s}}$. Since P4$^{\mathrm{s}}$-5$^{\mathrm{s}}$ is unstable, the trajectory departs from it and converges to ST4$^{\mathrm{s}}$. Phenomenologically, the ILM was attractively manipulated from $n = 5$ to $n = 4$.

The blue region in Fig. 13 tends to increase as the current I_{EM4} decreases. This implies that the impurity changes the phase structure around ST5$^{\mathrm{s}}$. Therefore, we conclude that attractive manipulation is a result of the change in the phase structure. In addition, the trajectory clearly shows that the behavior of the manipulated ILM was significantly affected by the phase structure around P4$^{\mathrm{s}}$-5$^{\mathrm{s}}$. Thus, we conjecture that the phase structure around the unstable P mode governs the behavior of the manipulated ILM. That is, the phase structure is the key to manipulating ILMs.

5. Conclusion

In this paper, a macro-mechanical cantilever array was proposed and modeled. The array consists of cantilevers, a coupling rod, an external excitor, and EMs. The EMs are placed beneath the cantilevers, producing a soft-spring nonlinearity. It was experimentally confirmed that the nonlinearity could be adjusted by changing the current flowing in the EMs. In addition, several ILMs were observed experimentally and numerically. The results suggest that the model describing the oscillation of individual cantilevers is valid. Therefore, a comparison of the numerical and experimental results suggests that the proposed cantilever array is a suitable system for the fundamental study of ILMs.

ILM excitation and attractive manipulation were demonstrated experimentally. ILMs were manipulated by reducing the current flowing in the EM, which induced an impurity. The impurity locally changed the resonant frequency of cantilevers. Thus, the amplitude of one cantilever increased after the addition of the impurity. If the amplitude became large enough, an ST mode remained after the impurity was removed. On the other hand, attractive manipulation was also observed by using an impurity. An ST mode was experimentally moved to the site where the impurity was added. That is, the ILM was attracted by the impurity. Attractive manipulation was confirmed by numerical simulations. However, a numerical simulation also showed that a stable P mode appeared after the impurity was removed. A stability analysis suggests that attractive manipulation of the ST mode is observed when the P modes are unstable. Thus, it is conjectured that the structure of the unstable manifold of unstable P modes determines the behavior of the manipulated ILM.

The macro-mechanical cantilever array makes it easy to investigate the control of ILMs in microscopic engineering if the scaling law is considered. The manipulation of ILM reported by M. Sato *et al.* have shown that the dynamics of ILM in micro-cantilever arrays can be described by a coupled ordinary differential equation, which is obtained by using the similar method to this paper [12]. This suggests that the qualitative investigation using our model equation can be applied to at least ILM in microscale mechanical structures. We will investigate the possibility of applying analyses using the macro-mechanical cantilever array to micro-engineering.

Acknowledgments

This work was supported by the Ministry of Education, Culture, Sports, Science and Technology in Japan, Grant-in-Aid for Young Scientist (B) No. 22760280.

References

[1] P. Binder, D. Abraimov, A.V. Ustinov, S. Flach, and Y. Zolotaryuk, "Observation of breathers in Josephson ladders," *Phys. Rev. Lett.*, vol. 84, p. 745, 2000.

[2] Thierry Cretegny, Thierry Dauxois, Stefano Ruffo, and Alessandro Torcini, "Localization and equipartition of energy in the β-FPU chain: Chaotic brethers," *Physica D*, vol. 121, p. 109, 1998.

[3] Thierry Dauxois, Michel Peyrard, and C.R. Willis, "Discreteness effects on the formation and propagation of breathers in nonlinear Klein-Gordon equations," *Phys. Rev. E*, vol. 48, p. 4768, 1993.

[4] H.S. Eisenberg, Y. Silberberg, R. Morandotti, A.R. Boyd, and J.S. Aitchison, "Discrete spatial optical solitons in waveguide arrays," *Phys. Rev. Lett.*, vol. 81, p. 3383, 1998.

[5] L.Q. English, F. Palmero, A.J. Sievers, P.G. Kevrekidis, and D.H. Barnak, "Traveling and stationary intrinsic localized modes and their spatial control in electrical lattices," *Phys. Rev. E*, vol. 81, p. 046605, 2010.

[6] S. Flach and C.R. Willis, "Discrete breathers," *Phys. Rep.*, vol. 295, p. 181, 1998.

[7] Jason W. Fleischer, Mordechai Segev, Nikolaos K. Efremidis, and Demetrios N. Christodoulides, "Observation of two-dimensional discrete solitons in optically induced nonlinear photonic lattices," *Nature*, vol. 422, p. 147, 2003.

[8] T. Hikihara, Y. Okamoto, and Y. Ueda, "An experimental spatio-temporal state transition of coupled magneto-elastic system," *Chaos*, vol. 7, p. 810, 1997.

[9] K. Kisoda, N. Kimura, H. Harima, K. Takenouchi, and M. Nakajima, "Intrinsic localized vibrational modes in a highly nonlinear halogen-bridged metal," *J. Lumin.*, vol. 94, p. 743, 2001.

[10] L.M. Marín and S. Aubry, "Breathers in nonlinear lattices: numerical calculation from the anticontinuous limit," *Nonlinearity*, vol. 9, p. 1501, 1996.

[11] R. Morandotti, U. Peschel, J.S. Aitchison, H.S. Eisenberg, and Y. Silberberg, "Dynamics of discrete solitons in optical waveguide arrays," *Phys. Rev. Lett.*, vol. 83, p. 2726, 1999.

[12] M. Sato, B.E. Hubbard, and A.J. Sievers, "*Colloquium*: nonlinear energy localization and its manipulation in micromechanical oscillator arrays," *Rev. Mod. Phys.*, vol. 78, p. 137, 2006.

[13] M. Sato, B.E. Hubbard, A.J. Sievers, B. Ilic, and H.G. Craighead, "Optical manipulation of intrinsic localized vibrational energy in cantilever arrays," *Europhys. Lett.*, vol. 66, (3) p. 318, 2004.

[14] M. Sato, B.E. Hubbard, A.J. Sievers, B. Ilic, D.A. Czaplewski, and H.G. Craighead, "Observation of locked intrinsic localized vibrational modes in a micromechanical oscillator array," *Phys. Rev. Lett.*, vol. 90, p. 044102, 2003.

[15] M. Sato and A.J. Sievers, "Direct observation of the discrete character of intrinsic localized modes in an antiferromagnet," *Nature*, vol. 432, p. 486, 2004.

[16] M. Sato, S. Yasui, M. Kimura, T. Hikihara, and A.J. Sievers, "Management of localized energy in discrete nonlinear transmission lines," *Europhys. Lett.*, vol. 80, p. 30002, 2007.

[17] A.J. Sievers and S. Takeno, "Intrinsic localized modes in anharmonic crystals," *Phys. Rev. Lett.*, vol. 61, p. 970, 1988.

[18] B.I. Swanson, J.A. Brozik, S.P. Love, G.F. Strouse, A.P. Shreve, A.R. Bishop, W.-Z. Wang, and M.I. Salkola, "Observation of intrinsically localized modes in a discrete low-dimensional material," *Phys. Rev. Lett.*, vol. 82, p. 3288, 1999.

[19] E. Trías, J.J. Mazo, and T.P. Orlando, "Discrete breathers in nonlinear lattices: Experimental detection in a Josephson array," *Phys. Rev. Lett.*, vol. 84, p. 741, 2000.

[20] A.V. Ustinov, "Imaging of discrete breathers," *Chaos*, vol. 13, p. 716, 2003.

[21] Philip S. Waggoner and Harold G. Craighead, "Micro- and nanomechanical sensors for environmental, chemical, and biological detection," *Lab Chip*, vol. 7, p. 1238, 2007.